A high entropy oxide as high-activity electrocatalyst for water oxidation

Mohana V. Kante[1], Daniel M. Cunha[2], Moritz L. Weber[3,4], Iris C. G. van den Bosch[2], Lisa Heymann[3], Emma van der Minne[2], Shu Ni[2], Lorenz J. Falling[4], Gertjan Koster[2], Felix Gunkel[3], Slavomír Nemšák[4], Horst Hahn[1], Leonardo Velasco[1,5,], Christoph Baeumer[2,3,]**

1 Institute of Nanotechnology, Karlsruhe Institute of Technology 76344 Eggenstein-Leopoldshafen, Germany.

2 MESA+ Institute for Nanotechnology, University of Twente, Faculty of Science and Technology, 7500 AE Enschede, Netherlands
3 Peter Gruenberg Institute and JARA-FIT, Forschungszentrum Juelich GmbH, 52425 Juelich, Germany
4 Advanced Light Source, Lawrence Berkeley National Laboratory, Berkeley, California 94720, USA
5 Universidad Nacional de Colombia sede de La Paz, Km 9 via Valledupar – La Paz, 202010 Cesar, Colombia

KEYWORDS: High-entropy oxides, Water electrolysis; Oxygen evolution reaction; Perovskite oxide catalysts, Green hydrogen

ABSTRACT

High entropy materials are a new pathway in the development of high-activity (electro-)catalysts because of the inherent tunability and coexistence of multiple potential active sites, which may lead to earth-abundant catalyst materials for energy-efficient electrochemical energy storage. In this report, we identify how the multi-cation composition in high entropy perovskite oxides (HEO) contributes to high catalytic activity for the oxygen evolution reaction (OER), i.e. the key kinetically limiting half-reactions in several electrochemical energy conversion technologies, including green hydrogen generation. We compare the activity of the (001) facet of $LaCr_{0.2}Mn_{0.2}Fe_{0.2}Co_{0.2}Ni_{0.2}O_{3-\delta}$ with the parent compounds (single B-site in the ABO_3 perovskite). While the single B-site perovskites roughly follow the expected volcano-type activity trends, the HEO clearly outperforms all of its parent compounds with 2.8 to 100 times higher currents at fixed overpotential. As all samples were grown as an epitaxial layer, our results indicate an intrinsic composition–function relationships, avoiding the effects of complex geometries or unknown surface composition. In-depth X-ray photoemission studies reveal a synergistic effect of simultaneous oxidation and reduction of different transition metal cations during adsorption of reaction intermediates. The surprisingly high OER activity demonstrates that HEOs are a highly attractive, earth-abundant new material class for high-activity OER electrocatalysts, possibly allowing fine-tuning the activity beyond the scaling limits of mono- or bimetallic oxides.

INTRODUCTION

Electrocatalysts are a key asset in the transition towards sustainability because they enable net-zero-carbon synthesis of value-added chemicals and chemical fuels, including power-to-X approaches.[1] One of the scientifically most-studied and technologically most important reactions is the oxygen evolution reaction (OER), e.g. for green hydrogen production through water electrolysis. This complex four-step reaction suffers from exceedingly large overpotentials.[2] A key limitation is the linear scaling relation between the energy of different reaction intermediates (and their transition states).[3–6] Specifically, the reaction intermediates HOO* and HO* (* denotes the active site) exhibit the same dependence on the nature of the active site.[3] The resulting linear scaling of their adsorption energies inherently leads to an "overpotential wall" which must be overcome to maximize OER efficiency.[7]

Perovskite-type transition metal oxides (ABO_3) are of special interest as OER electrocatalysts because of high activities in alkaline media even without the use of platinum-group metals and their tunability of physical and electrochemical properties through substitutional doping of the A and B sites.[8–14] This tunability is key to optimize the catalyst activity, but perovskite oxides still face the overpotential wall resulting from the linear scaling.[3] To overcome this scaling, so-called high entropy materials were proposed as alternative future OER electrocatalysts. High entropy materials are single-phase multicomponent systems of five or more elements, typically with near-equiatomic concentrations. The multitude of available lattice sites in these materials enables rapid screening for ideal (local) composition with optimized active site properties, e.g. the relative energy levels available for catalysis.[15–17] The close proximity of multiple possible active sites has even been suggested as a new pathway to overcome scaling relations because of different preferred adsorption sites for individual OER steps.[7,18] The overall thermodynamic barriers of the catalytic cycle on a high entropy material may thus be decreased through the availability of different energy levels for the individual OER steps on different adsorption sites. Accordingly, metallic high entropy alloys have already shown great promise for the OER.[15–18] For earth-abundant transition metal high entropy alloys, complex oxide or hydroxide layers form at the surface, which lead to extremely low overpotentials and Tafel slopes (~300 mV at 10 mA cm^{-2} and 29 mV dec^{-1} in 1 M KOH),[19,20] indicating significant activity enhancement compared to standard benchmarks like IrOx or Ni/Fe layered hydroxides/oxyhydroxides.[21]

Recent advances in material synthesis[22,23] now enable the fabrication of high-entropy oxides (HEOs), i.e. single-phase metal oxides with five or more metal cations on the same crystallographic site. Compared to high-entropy metal alloys, the presence of additional sublattices in HEOs allows dedicated engineering of physical materials properties. For example, rich magnetic properties are available through an increase in the number of microstates available to the macroscopic system,[24] and the mixed oxygen-transition metal orbital character and covalency of the employed electronic states allows further fine-tuning of the adsorption energies and charge transfer characteristics,[25–27] or even an oxygen-related active site for electrocatalysts.[28] Accordingly, HEOs already showed high promise as battery electrodes[29] and as (electro-)catalysts.[30–32] The realm of HEOs was extended to perovskite oxides in 2018,[22,33] which offer combining the promising properties and catalytic performance of high-entropy materials with the established high-activity platform of transition metal perovskite oxides. Despite very recent first accounts on HEO perovskite OER electrocatalysts,[28,34] the electrocatalytic activity has not yet been systematically explored and separated from complex morphologies resulting from the employed synthesis methods or from self-assembly of oxide layers at the solid/liquid interface.[19,20,34,35]As the Jaramillo, Nørskov, Rossmeisl and Markovic groups argued already in 2011 and 2017, the comparison of intrinsic activity across multiple compositions should be performed on identical sample geometries and ideally on single crystalline surfaces.[3,36] This approach is even more important for high entropy electrocatalysts, where the complexity in composition, structure and physical properties has been the main hurdle in understanding of structure-activity relationships.[37]

In this report, we explore the OER activity of the (001) facet (using the pseudocubic notation) of a perovskite oxide (P-HEO) with five B-site transition metal cations with equiatomic concentration, $LaCr_{0.2}Mn_{0.2}Fe_{0.2}Co_{0.2}Ni_{0.2}O_{3-\delta}$ (Figure 1a). Cr, Mn, Fe, Co and Ni are chosen as B-site cations because they span a wide range of binding energies in the activity volcano of the parent compounds (single B-site).[3] This P-HEO is synthesized as an epitaxial thin-film, which allows deriving structure–function relationships between the reactivity and the atomic-level surface structure and composition of a defined crystallographic facet.[9,36,38] Using epitaxial thin-films avoids the effect of complex geometries and the need for carbon-containing binders.[39,40] We compare the P-HEO OER activity to epitaxial layers of the parent perovskite compounds and find that P-HEO exhibits drastically enhanced activity, with a factor 2.8 to 100 enhancement at fixed overpotential. These findings suggest that HEOs are a new candidate material class for high-activity OER electrocatalysts, possibly allowing fine-tuning the activity beyond the scaling limits of mono- or bimetallic oxides, and urgently calling for mechanistic studies to investigate the origin of the activity-enhancement for further electrocatalyst optimization.

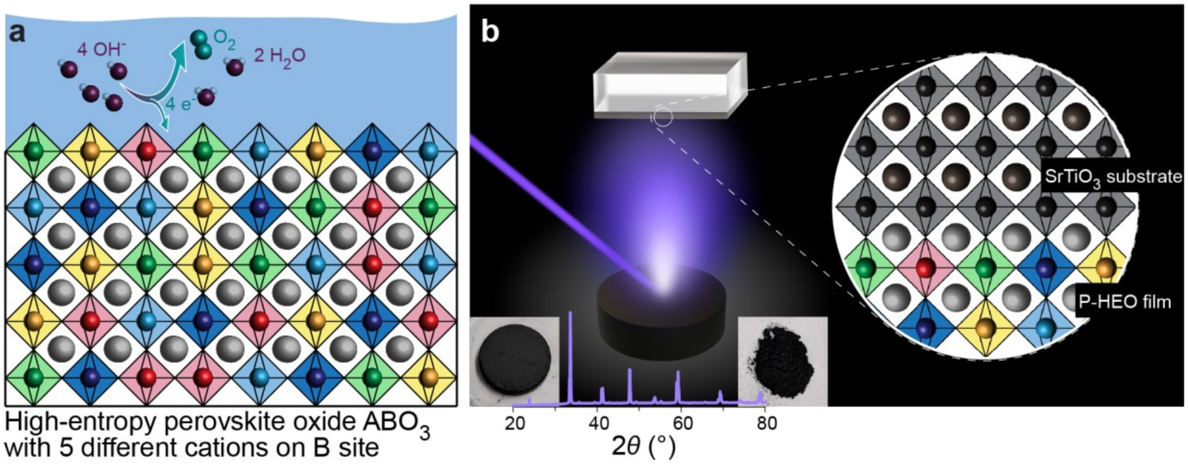

Figure 1: (a) Schematic illustration of the P-HEO electrocatalyst for water electrolysis. (b) The epitaxial layer is deposited via PLD. The PLD target is synthesized via sintering of P-HEO powder using reverse co-precipitation followed by calcination (see experimental section). The insets show optical micrographs of the powder and the sintered target and an X-ray diffractogram of the target, which confirms the single-phase perovskite structure, as detailed in our previous work.[22]

RESULTS AND DISCUSSION

To assess the electrocatalytic activity of a well-defined, single crystallographic facet of the recently developed P-HEO, we synthesized epitaxial layers of P-HEO via pulsed laser deposition (PLD, Figure 1b) from a self-made ceramic target. The PLD parameters were chosen similar to the description in ref. [24], see experimental details. P-HEO films with 12 nm thickness show a comparably smooth surface morphology with a root mean square (RMS) roughness of ~300 pm (Figure 2a). X-ray reflectivity (XRR) confirms that the film has a thickness of ~12 nm (Supplementary Figure 1). High resolution X-ray diffraction (HRXRD, Figure 2b-c) exhibits clear Laue fringes, indicating the high crystalline quality of the P-HEO film. The P-HEO film peaks are seen as broad features overlapping with the substrate peaks, indicating similar lattice parameters for film and substrate (~3.9 Å). X-ray photoelectron spectroscopy with varying mean escape depth *d* revealed that the surface was slightly deficient in Ni, Co and Fe, indicating predominant A-site termination (Supplementary Figure 2).[41] Interestingly, the 12 nm P-HEO film does not exhibit

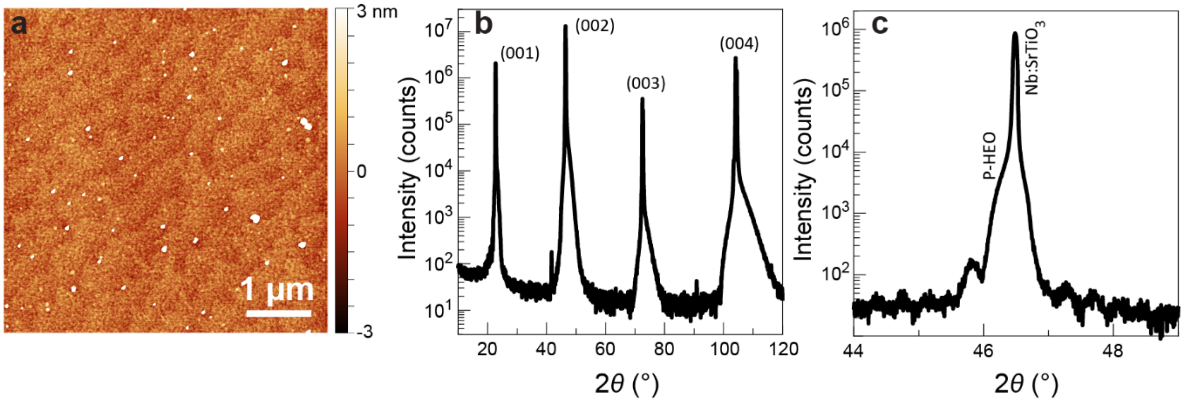

Figure 2: (a) AFM morphology of a 12 nm P-HEO deposited on a Nb:$SrTiO_3$ substrate. (b) and (c) XRD patterns of the same P-HEO film, indicating epitaxial growth of the HEO thin film in (001) orientation of the perovskite structure. Small peaks at ~ 41.6 and 90.5° correspond to Cu K_β diffraction of the substrate.

measurable electrical conductivity at room temperature (the resistance was higher than 10 MΩ), as was also observed before.[24]

Transmission electron microscopy investigation of the film/substrate interface is shown in Figure 3, confirming a coherent P-HEO layer on the substrate, as expected from HRXRD. The film shows a well-ordered crystal structure with occasional extended defects, not unexpected for complex oxide thin films fabricated by PLD.[42] The sharp interface between the substrate and the film is visible through the Z-contrast in high annular angle dark-field (HAADF) imaging conditions and the film shows an epitaxial relation to the substrate (Figure 3a). The fast Fourier transform (FFT) of Figure 3a, which includes both the film and the substrate, exhibits a spot pattern (Figure 3b) that lies on 100 zone axis, and the high resolution TEM image in Figure 3c confirms the well-ordered crystal structure.

An energy-dispersive X-ray spectroscopy (EDX) chemical composition map containing the substrate and the film is displayed in Figure 3d. It is evident that the interface between the substrate and the film is sharp (limited intermixing) and that there is no significant segregation of specific elements at the nanoscale. The chemical composition mapping of the film (Table 1) shows that all

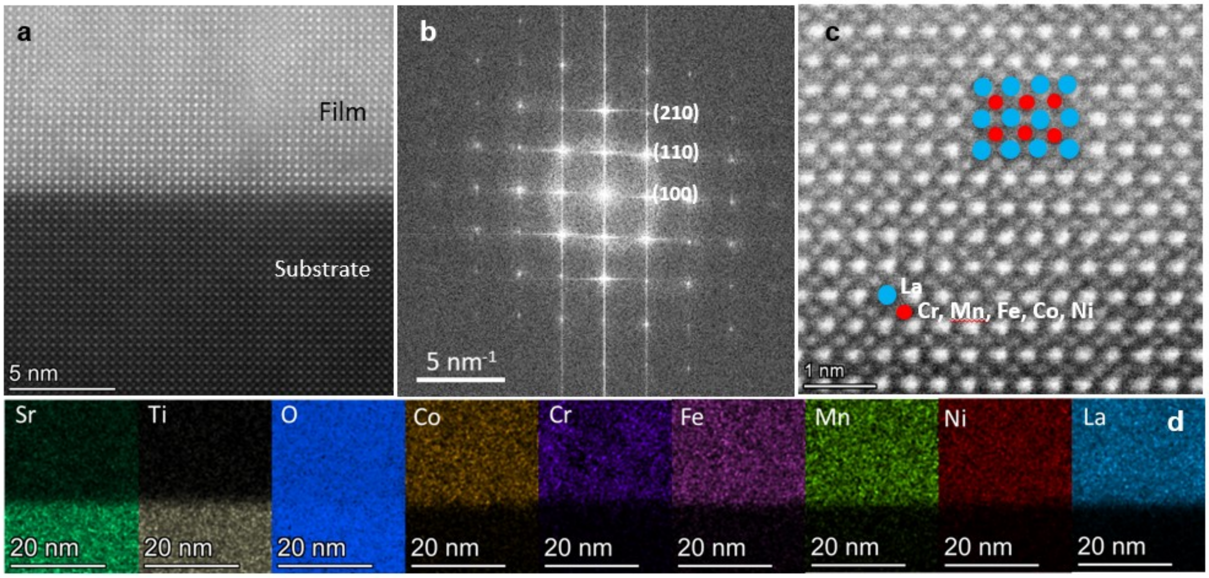

Figure 3: (a) TEM micrographs of the interface of the P-HEO film and the substrate (b) Fast Fourier transform (FFT) of (a). (c) Magnified view of TEM micrographs of the P-HEO film. (d) EDX chemical composition maps of the film and the substrate.

the transition metals are in near equiatomic composition, confirming near-stoichiometric transfer from the PLD target to the thin film. The mapping was repeated in several locations, confirming the homogeneous composition. To summarize, our observations with HRXRD, XRR and TEM suggest that the film has a single phase with epitaxial growth and a lattice parameter of ~3.9 Å, indicating a slight lattice expansion based on a pseudo-cubic bulk lattice parameter of 3.87 Å.[24] Moreover, no segregation phases or compositional inhomogeneities were detected in the TEM analysis.

Electron energy loss spectroscopy (EELS) was used to analyze the oxidation states of the constituent elements by examining the edge position and ratio of the L_2- and L_3-edges of Cr, Mn, Fe, Co and the ratio of the M_4- and M_5-edges for La (see Supplementary Figure 4 for the EELS data). The intensity ratios (I_{L3}/I_{L2} or I_{M5}/I_{M4}) indicate that the oxidation states of Cr and Fe is +3,[43,44] while Mn exhibits a slightly reduced +3/+2 valence,[44,45] and Co shows stronger reduction towards +2 valence. These oxidation states are in agreement with the expected charge transfer and preferred

Table 1: Atomic fraction from EDX, position of the energy edge, intensity ratio of the edges (I_{L3}/I_{L2} or I_{M5}/I_{M4}) and oxidation states of corresponding elements in the system, as estimated from the edge position and intensity ratios.

Element	**Atomic fraction from EDX (%)**	**Position of L_3 EELS edge (eV)**	**Intensity ratio**	**Oxidation state from EELS**
Cr	9.0±1.3	574	1.68	+3[43]
Mn	9.7±1.7	637.7	2.96	Mostly +3 (small +2 contribution) [44,45]
Fe	10.9±1.9	706.2	4.78	+3 [45]
Co	10.1±2.0	776	4.36	Mostly +2 (small +3 contribution) [44]
Ni	9.9±1.9			
La	50.6±8.3	832	0.85	+3

valence states in the first row transition metals.[46,47] Lanthanum only exhibits +3, as expected from the stable inert gas La^{+3} configuration. The Ni L-edge at 850 eV is not interpretable due to the strong overlap by the La M-edge.[48] The TEM/EELS analysis confirms that our P-HEO has the desired perovskite phase, in contrast to previous reports that exhibited pronounced Cr deficiency.[34] The slight reduction of Mn and Co (and possibly of Ni) may be the result of a small oxygen deficiency due to favorable reduction enthalpy, as is frequently observed in the single B-site perovskites, especially with increasing degree of covalency.[26]

To compare the OER activity of the epitaxial P-HEO with its single B-site parent compounds, (001)-oriented PLD films of $LaCrO_3$, $LaMnO_3$, $LaFeO_3$, $LaCoO_3$, and $LaNiO_3$ were grown by PLD. The films of all compositions showed two-dimensional growth resulting in a smooth surface with RMS roughness below 300 pm (Supplementary Figure 7-11). All films exhibited predominant A-site termination, as revealed by X-ray photoelectron spectroscopy (XPS) analysis. While we recently demonstrated that the surface termination can have large effect for the OER activity,[12] this observation allows direct comparison of the OER activity as a function of film composition. With these epitaxial, single-phase and well-ordered (100)-oriented thin films, we are thus well-positioned to systematically assess the intrinsic OER activity of the P-HEO.

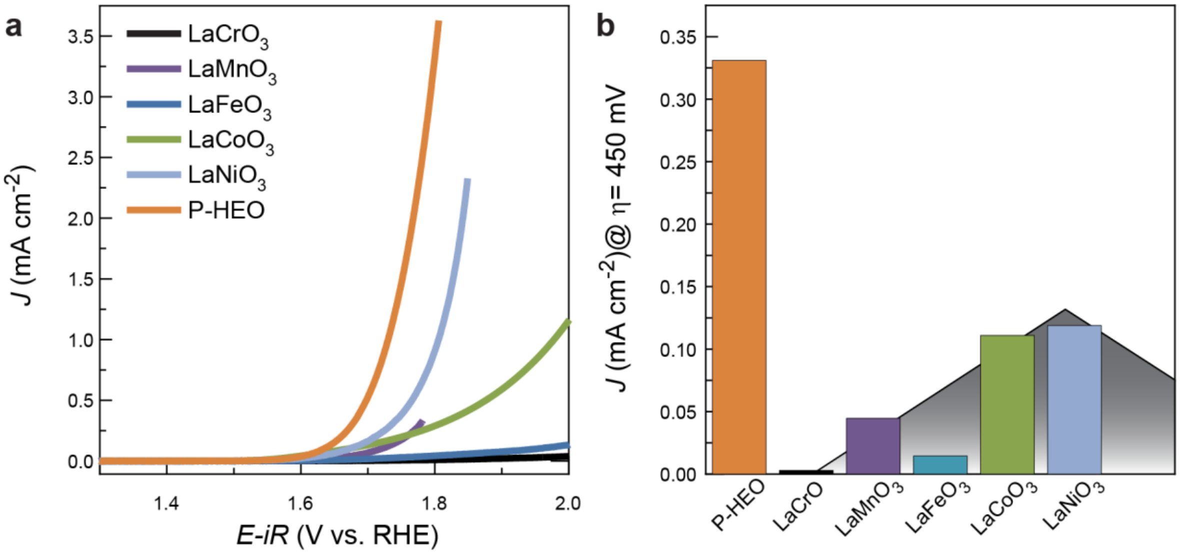

Figure 4: (a) Cyclic voltammetry of P-HEO and the parent compounds. The plots show the average of anodic and cathodic scans in the second consecutive cycle. (b) Comparison of the specific OER activities (current density at an overpotential of 450 mV, i.e. 1.68 V vs RHE). The underlying volcano is a guide-to-the-eye, inspired by the predicted activity volcano from ref. [49].

OER activity was measured using cyclic voltammetry (CV) in O_2-saturated 0.1 M potassium hydroxide (KOH) solution in three-electrode configuration using a specially designed rotation disk electrode (RDE) setup for epitaxial thin films.[12] Electrical contact was ensured through a sputtered Pt contact on the film edges and through a highly-conductive Nb:$SrTiO_3$ substrate. Figure 4a shows the average of the anodic and cathodic scans for the films with different compositions, indicating that P-HEO possesses higher OER activity than all single B-site parent compounds. The single B-site perovskite oxides roughly follow the volcano-shaped trend predicted from DFT (Figure 4b),[49] which results from increasing energy difference between O* and HO* intermediates with increasing electronegativity of the transition metal,[3] with the exception of $LaFeO_3$, which showed a lower activity than expected based on this trend. The P-HEO activity is approximately 3 times higher than for $LaNiO_3$ and $LaCoO_3$, approximately 7.5 times higher than for $LaMnO_3$ and more than 100 times higher than for $LaCrO_3$ at the reference overpotential of 450 mV. Similar activity trends were also observed in a previous study, which compared samples with high surface roughness and unknown surface composition and orientation.[34] This further verifies our observation of remarkable activity increase, while our results with epitaxial thin films have the distinct advantage of confirming intrinsic materials trends. The surface area for all our films is well represented with the geometric surface area because of the negligible surface roughness. The tensile strain state and crystalline quality of the P-HEO film is also similar to the more active parent compounds $LaNiO_3$ and $LaCoO_3$ thin films. If we assume only one active site, lower rather than higher activity would be expected for P-HEO because the presumed active sites (i.e., one of the transition metal ions with 3+ or mixed 2+/3+ oxidation state) are also present in the parent compounds, but with a higher concentration.

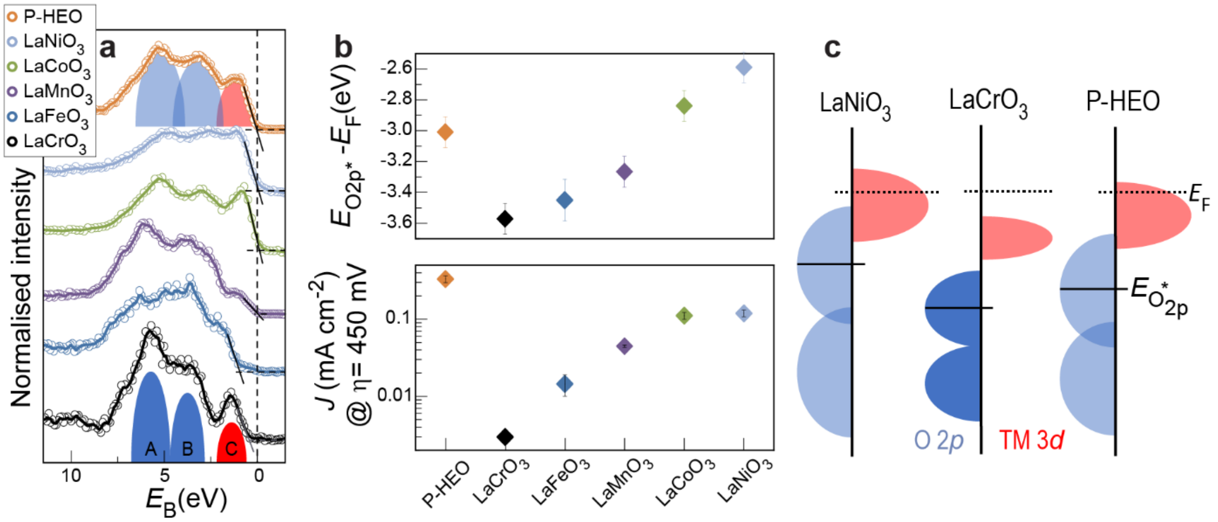

Figure 5: (a) Valence band spectra of P-HEO and parent perovskite oxides. The intensity was normalized to the area of the binding energy region -2 to 8 eV. Oxygen O 2*p* states (peaks A and B, blue) and TM 3*d* states (peak C, red) are schematically for the examples of $LaCrO_3$ (low degree of covalence) and P-HEO (high degree of covalence). Raw data is shown as open dots, lines are a guide to the eye obtained by 5-point adjacent average smoothing. The valence band maximum (VBM) is indicated via the zero-photoemission intensity intercept of a linear regression fit of the low- binding-energy edge of the valence band spectra. (b) O 2*p* non-bonding state binding energy $E_{O_{2p}}$ and OER activity for P-HEO and parent perovskite oxides. The error bars represent the possible maximum deviation of the consecutive measurements (top panel) or estimated relative errors from triplicate CV measurements (bottom panel). Note that the parent compounds are ordered by $E_{O_{2p}}$ rather than atomic number of the TM. (c) Schematic energy band diagram for $LaNiO_3$, $LaCrO_3$ and P-HEO. The Fermi level (E_F) is labeled by dashed lines in (a) and (c) and the valence band maximum is schematically shown as linear extrapolation of the leading edge of the VB.

To clarify possible origins of the surprisingly enhanced activity, we examine the electronic structure of P-HEO in more detail using valence band spectroscopy (Figure 5a-c). The binding energy was calibrated using the C 1*s* peak and only small errors (< 0.2eV) are expected because charging is negligible in such thin films on highly conductive substrate. The valence band structures of the parent compounds are similar to previous results obtained on perovskite powders,[50] consisting of bonding O $2p$ states (peak A in Figure 5a,c), non-bonding O $2p$ states (peak B) and TM $3d$ states (peak C). In previous studies, the measured charge-transfer energy (the difference in energy between the occupied O $2p$ band center and unoccupied TM $3d$ orbitals)[27] or the computed O $2p$ band center[51] were used as activity descriptors for perovskite-type OER electrocatalysts. To assess the O $2p$ band position experimentally, we fitted the valence band spectra using Voigt functions after Shirley background subtraction (Supplementary Figure 3). Our parent perovskite oxides $LaCrO_3$, $LaMnO_3$, $LaFeO_3$, $LaCoO_3$, and $LaNiO_3$ exhibit a direct correlation between the measured peak position of the non-bonding O $2p$ states ($E_{O_{2p}}$, with respect to the Fermi level) and the OER activity (Figure 5b, Supplementary Figure 12). Among the parent compounds, $LaNiO_3$ is the most active for the OER and exhibits the highest $E_{O_{2p}}$, as well as the smallest energy difference between O $2p$ and occupied TM $3d$-states. Together with a broadening of the O $2p$ bands, this results in a higher overlap of O $2p$ and TM $3d$ bands, corresponding to higher covalency of the TM−O bonds. It is believed that the TM $3d$–O $2p$ hybridization and large total bandwidth are the reason for high OER activity.[11,25] In contrast, $LaCrO_3$ shows the lowest $E_{O_{2p}}$, a large energy separation and thus a small overlap of O $2p$ and TM $3d$ bands, indicating the lowest covalency in this series. In addition, $LaCrO_3$ ($LaMnO_3$, $LaFeO_3$) show negligible (small) density of states near the Fermi level, indicating that insufficient electronic conductivity may further contribute to the low OER activity. The valence band structure data can also explain why

$LaFeO_3$ was less active compared to the expected trend (Figure 4b). The increase in exchange stability in the $3d^5$ configuration of $LaFeO_3$ leads to an increase in charge transfer gap and decrease in hybridization compared to the trend of 3d TM perovskites.[50] Accordingly, we recover a monotonic trend when plotting the OER activity as a function of $E_{O_{2p}}$ (Figure 5b).

For P-HEO, we find a valence band signature that resembles the highly covalent parent compounds. P-HEO has a large bandwidth and TM $3d$–O $2p$ hybridization (Figure 5a). Figure 5c shows a schematic illustration of the valence band contribution of TM $3d$ and O $2p$ states. The binding energy for non-bonding O $2p$ states is lower than for $LaCoO_3$ and $LaNiO_3$ but higher than for $LaCrO_3$, $LaMnO_3$ and $LaFeO_3$ (Figure 5b). Despite the high in-plane electronic resistance measured in van-der-Pauw geometry, the P-HEO exhibits a substantial density of states near the Fermi level, which was previously shown to be sufficient for high-activity perovskite OER catalysts.[11] Based on typical OER descriptors, the valence band structure of P-HEO thus suggests mediocre OER activity (lower activity than $LaNiO_3$, lower or on par with $LaCoO_3$). Therefore, the experimentally observed substantially increased activity compared to $LaNiO_3$ shows that neither electronic structure descriptors nor simplistic arguments regarding the availability of active sites can explain the OER activity of this P-HEO. Instead, active sites and local, partial reactions of the four-step OER must be considered in a holistic or even synergistic picture, lending support to previous arguments that the unique arrangement of the surrounding of a given binding site tunes the electronic properties of this site,[15,52] or that two different neighboring active sites may synergize for subsequent steps in the catalytic cycle and therefore “stabilize OER intermediates that are unfavorable” on single sites.[53] Such a scenario might be particularly important when considering decoupled electron-proton transfer OER mechanisms,[54,55] and has also been discussed in other multi-cation oxide electrocatalysts.[56]

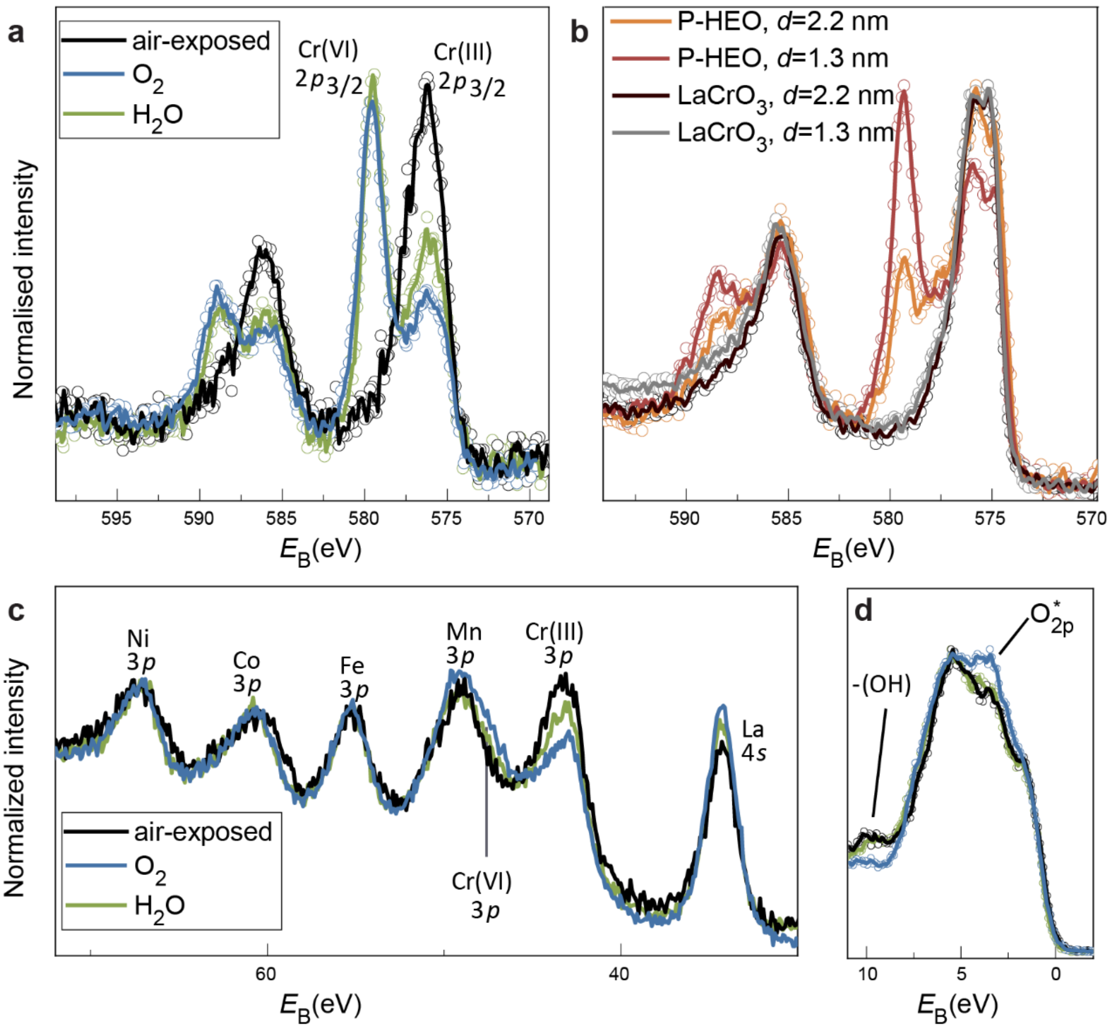

Figure 6: (a) Cr 2*p* core level of P-HEO during APXPS experiments. (b) Cr 2*p* core level of P-HEO with different mean escape depth *d*. Cr 2*p* core level of $LaCrO_3$ are shown for reference. Spectra collected in UHV after annealing in O_2 . (c) TM 3*p* core levels of P-HEO during APXPS experiments. (d) VB spectra of P-HEO during APXPS experiments. Raw data in (a),(b),(d) is shown as open dots, lines are a guide to the eye obtained by 5-point adjacent average smoothing.

To shed light on the role of the different cations in P-HEO for the binding of hydroxyl groups, a key step for all suggested OER mechanisms in alkaline media, we employed ambient pressure XPS (APXPS) analysis.[54,57] For *in-situ* measurements, the samples were cleaned by 300 °C annealing in O_2 before exposure to an H_2O ambient at 25 °C. The cleaned surface represents the as-prepared state (not exposed to air) because the synthesis ends with annealing and cooling down in O_2. After the annealing, the Cr 2*p* and Cr 3*p* levels are indicative of a large Cr^{6+}

contribution, while after air exposure, we only find Cr^{3+} (Figure 6a,c). Measuring the same sample with different mean escape depths after annealing (Figure 6b) confirms that the oxidation is confined to the top surface of the P-HEO film. We also note that such surface oxidation does not occur for $LaCrO_3$ films (Figure 6b) unless treated with ozone or oxygen plasma.[58] These results thus indicate that oxidation of Cr is more facile in the P-HEO than in the parent perovskite. The oxidation of Cr is accompanied by an oxidation in Ni and Co as is qualitatively evident from the peak shift and low-binding energy shoulder in the $3p$ core level,[11] while the Mn and Fe valence state remain unchanged within experimental resolution (Figure 6c). Judging from previous TM $3p$ measurements,[11] the average Ni valence increases by ~0.1, and the average Co valence increases by ~0.3 during Cr oxidation. The simultaneous Cr and Co oxidation is also confirmed by XAS experiments under the same conditions (Supplementary Figures 5,6), indicating that binding of surface species (including OER reaction intermediates) results in a collective response from the different TM cations. The adsorption of HO* is also evident in the valence band spectra of P-HEO, where exposure to both ambient and water vapor lead to the development of a clear -OH peak and a decrease in intensity of non-bonding O $2p$ states (Figure 6d), further highlighting the importance $E_{O_{2p}}$. The charge transfer direction still follows the expected trend with reduction for the more electronegative transition metals.[46] The Ni valence change is barely visible within our experimental XPS resolution and cannot be tracked by soft X-ray XAS because the Ni L-edge overlaps with the La M-edge, which is much higher in intensity. The Ni valence change will thus not be discussed in more detail because the changes in Co valence are more pronounced.

When the O_2-annealed surface is exposed to H_2O vapor in the APXPS experiment, the changes in oxidation state are partially reversed: Cr is reduced (Figure 6a,c). A Co oxidation is evident in the XAS signature (Supplementary Figure 6), while no large change is appreciable in the Co $3p$ XPS core level. The Mn and Fe valence state remain unchanged within experimental uncertainty. All spectral changes are smaller compared to air-exposure, which can be rationalized by the lowp_{H_2O} in the APXPS experiment and the absence of other species that may bind to the surface like carbonate groups. It was previously observed that oxide OER electrocatalysts benefit from the presence of Cr^{6+} ions, but their role for OER is not yet fully understood.[59] For P-HEO, the Cr (and to some degree Co) valence changes are directly connected to the adsorption of HO* and these cations have a strong tendency for facile changes in the oxidation state. The preferential valence change of Cr alongside much smaller changes in other TM oxidations states may indicate a synergistic effect in the binding of surface adsorbates, a possible reason for enhanced OER activity. One may therefore speculate that the Cr and Co cations play an integral role in the OER mechanism in this class of P-HEO electrocatalysts and that the presence of easy-to-oxidize Cr in the HEO matrix contributes to high OER activity. The presence of multiple cations with different electronegativity and ease of oxidation apparently facilitates both the initial bonding of HO* and the following oxidation steps, which would present a deviation from the often observed scaling relations. In the framework of the Sabatier principle (optimum activity if reaction intermediates bind neither too weakly nor too strongly), one may speculate that Cr active sites may have a low thermodynamic barrier for the initial oxidation (HO* to O* in the adsorbate evolution mechanism), while Ni and Co have a lower thermodynamic barrier for additional oxidation steps (e.g. O* to HOO*), leading to a synergistic effect of adjacent TM sites of the P-HEO.[3]

CONCLUSIONS

In conclusion, our findings reveal that the (001) facet of the P-HEO $LaCr_{0.2}Mn_{0.2}Fe_{0.2}Co_{0.2}Ni_{0.2}O_{3-\delta}$ is highly active for catalyzing the OER. Our study provided a one-to-one comparison of the same crystallographic facet with close to identical morphology and surface termination for a range of perovskite oxides. While the single B-site perovskites follow the OER trend expected based on the binding energy of non-bonding O 2*p* states, in reasonable agreement with DFT-predicted activity trends, the new class of P-HEO electrocatalysts clearly outperforms all of its single-B parent compounds. Our valence band analysis showed that the electronic structure of P-HEO is of a highly covalent nature, which is beneficial for OER activity. But the activity of P-HEO is higher than expected from electronic structure considerations. APXPS analysis showed that on adsorption of reaction intermediates, several transition metals exhibit a valence change, indicating a synergistic effect in the binding of surface adsorbates, which may be the cause of the enhanced OER activity. These findings necessitate detailed future clarification of the OER mechanism on P-HEO materials and possible synergistic roles of multiple active sites to enable further electrocatalyst optimization based on rational design rules and advanced materials synthesis, as well as dedicated compositional screening for optimized synergistic effects between different cations. Furthermore, we note that the magnetic moment of the active sites may play a crucial role in the formation of the oxygen molecule, which possesses a triplet ground state.[60] This will be an important point of consideration for future investigation of high entropy oxygen electrocatalysts. Our conclusions provide a new stimulus in the field of HEOs to explore and exploit high entropy electrocatalysts for fundamental research as well as in application. In this sense, high entropy oxides provide a surprisingly active addition to the recent shift towards high-entropy OER electrocatalysts.

METHODS

Thin film preparation. High entropy $LaCr_{0.2}Mn_{0.2}Fe_{0.2}Co_{0.2}Ni_{0.2}O_{3-\delta}$ films of 12 nm and 70 nm were deposited on (001)-oriented $Nb:SrTiO_3$ substrates (0.5 wt%) via PLD. The PLD target was synthesized via sintering of perovskite powder using reverse co-precipitation followed by a calcination process. The powders were annealed at 1200˚C for 7 h, followed by uniaxial-pressing at 300 MPa and a heat treatment at 1500˚C for 12 h.[61] The P-HEO films were deposited with a laser fluence of 1.6 J/cm^2 and a frequency of 1 Hz at an oxygen pressure of 0.05 mbar and the temperature of the substrate was kept at 750 ˚C during deposition. The distance between sample and target was kept at 2.5 cm and the laser spot size was 0.04 mm^2. The aperture for laser entry during PLD was kept at 7 mm. After deposition, the sample was annealed inside the PLD at 750 ˚C and 100 mbar oxygen pressure for 10 mins.

Single B-site thin films were deposited on TiO_2-terminated and step-terraced $Nb:SrTiO_3$ substrates (0.5 wt%, etched with buffered hydrofluoric acid, followed by annealing in oxygen at 950 °C for 2 h). PLD was performed in a vacuum system with a base pressure of $2 \times 10{-}8$ mbar, equipped with an in situ RHEED and a KrF excimer laser of 248 nm. The central part of the laser beam was selected with a rectangular mask, resulting in a spot size: of 1.92 mm^2 on polycrystalline targets of desired composition. The optimized growth parameters per material (substrate temperature, laser repletion rate, spot size, laser fluence, substrate-target distance, O2 background pressure, obtained growth rate) are summarized in Supplementary Figures 7-11.

Thin film characterization. Surface morphology was investigated using atomic force microscopy (AFM), with a Bruker Dimension ICON (USA). Roughness was determined as RMS roughness of a line profile along a step edge.

X-ray reflectivity (XRR) and high resolution X-ray diffraction (HRXRD) were conducted in a Bruker AXS D-8 X-ray diffractometer with a monochromated Cu source to characterize the crystallinity of the films. Additional XRD measurements were performed on a Panalytical X'pert Pro MRD with a nonmonochromated Cu source, using of a nickel filter to remove the K_β emission. XPS measurement were conducted with an Omicron XM 1000 MkII Al K_α monochromated X-ray source and an Omicron EA 125 energy analyzer. The mean escape depth d is defined through the inelastic mean free path of photoelectrons $\lambda = 2.2$ nm (calculated via QUASES-IMFP-TPP2M)[62] and the photoemission angle θ through$d = \lambda \times cos\theta$[63], photoemission angles used are 0° and 55°. This isotropic approach uses the straight-line approximation,[64] as is suitable in the absence of well-characterized, material-specific angle-dependent effective attenuation lengths. For a full description of the information depth in photoemission, the readers are referred to refs. [63–65]. To calculate the surface stoichiometry from the measured intensities, we compared the relative intensity of the A-site and B-site peaks as a function of d. The stoichiometry was determined based on the integrated raw peak areas after subtraction of a Shirley background using CasaXPS. For analysis of the valence band, the binding energy was calibrated by shifting the C 1*s* peak of the adventitious carbon layer to 284.8 eV.

A Focused ion beam (FEI strata 400) (FIB) was used to extract cross-section lamellas for transmission electron microscopy (TEM) characterization, following procedures described elsewhere [66]. TEM characterization was conducted along the cross-section of the films in a Themis-Z (ThermoFischer). A Super-X EDX detector was used to analyse the chemical composition of the films, while EELS data was collected using a Gatan GIF Continuum 970 High resolution camera.

Electrical resistivity was measured in van der Pauw geometry after sputtering of gold contacts in all 4 corners of the sample. Additional testing was performed with by connecting the gold contacts to a multimeter.

Electrochemical characterization. To perform electrochemical experiments with epitaxial thin films on 10×10×0.5 mm^3 single crystal substrates, we used a custom-made adapter to press the sample back side to the Pt plug of a rotating disk electrode (RDE, Pine Research). 50 nm Pt connections from the sample back side to the front side ensured electrical contact to the Nb:$SrTiO_3$ substrate and the epitaxial layers. On the front side, a film area of 0.75 mm diameter was exposed to the electrolyte and sealed using an O-ring (Kalrez, ERIKS, Germany). The RDE shaft was rotating at 1600 rpm. Electrochemical testing was performed using a Parstat 4000 potentiostat (Cyclic voltammetry sweep rate 10 mV/s), in a 150-mL alkaline-resistant Teflon cell (Pine Research) with a Pt wire as a counter electrode. Electrochemical impedance spectroscopy (EIS) was conducted with the amplitude of 10 mV at open circuit potential and the correction for the cell resistance (IR correction, typically 45-55 Ω) was based on the high-frequency intercept of the real impedance. The electrolyte solution of 0.1 M KOH, prepared by dissolving KOH pellets (Sigma-Aldrich, 99.99%) in deionized water. The electrolyte was O_2-saturated prior to testing for at least 30 minutes and maintained under O_2 atmosphere during testing. All electrochemical measurements were performed at room temperature, following the recommended practices for comparison and benchmarking of model electrocatalyst systems.[67] Potentials were referenced to a Hg/HgO reference electrode (C3 Prozess- und Analysentechnik, Germany), which was periodically calibrated to the reversible hydrogen electrode (HydroFlex, USA) in 0.1 M KOH with typical values of ~890 mV. All OER testing was performed on a fresh electrode that had not undergone previous testing. Cyclic voltammetry was first performed in the pseudocapacitive redox phase change region (~0.9 to 1.75 V vs. RHE) at scan rates between 10 and 500 mV s^{-1}, followed by OER testing performed from 0.9 to 1.9 V vs. Hg/HgO at a scan rate of 10 mV s^{-1}. For $LaMnO_3$, unstable behavior was observed for potentials exceeding 1.75 V vs. RHE, so only data below 1.73 V vs. RHE was reported. The CV data was capacitance corrected through averaging the forward and backward scans. The second cycle is shown for each sample.

Ambient pressure XPS. Ambient pressure X-ray photoelectron spectroscopy was performed using the soft X-ray beamlime 9.3.2 at the Advanced Light Source, Lawrence Berkeley National Laboratory with a photon energy of 750 eV. The measurements were carried out in the as-received state of the thin-film at UHV conditions as well as under exposure of the sample with $p(O_2) = 75$ mTorr at $T = 300$°C, and subsequently, at $p(H_2O) = 75$ mTorr at room temperature. The H_2O reservoir was prepared from deionized water (Millipore, > 18.2 MΩ cm) and degassed by three consecutive freeze–pump–thaw cycles. For each sample state, a full set of La 4*d*, Cr 2*p*, Mn 2*p*, C 1*s*, O 1*s* as well as the shallow core-level region including the valence band was recorded. The respective partial pressures of the O_2 and H_2O atmosphere were adjusted at room temperature and the measurements were started approximately 20 min after the probing conditions have stabilized (and the C 1s contribution has vanished upon O_2 annealing). The heating rate in O_2 environment was ~50°C/min, while the cooling rate was ~10°C/min. Evaluation of the XPS spectra was performed using KolXPD.

ASSOCIATED CONTENT

Supporting Information. Additional XPS, XAS, XRD and AFM analysis.

AUTHOR INFORMATION

Corresponding Author

* Corresponding authors: c.baeumer@utwente.nl; lvelascoe@unal.edu.co

Author Contributions

F.G., H.H., L.V. and C.B. conceived and designed the experiments. M.V.K., D.M.C., L.H. and C.B. synthesized the samples. M.V.K., D.M.C., I.B., L.H. E.M., S.Ni and L.V. performed and analyzed physical characterization measurements. I.B. and C.B. performed and analyzed the electrochemical experiments. M.L.W., S.N. and C.B. performed and analyzed the (AP)XPS experiment. G.K., F.G., S.N. H.H., L.V. and C.B. supervised the research. M.V.K., L.V. and C.B. wrote the manuscript with contributions from all authors. All authors have given approval to the final version of the manuscript.

Funding Sources

Support from the University of Twente in the framework of the tenure track start-up package is gratefully acknowledged. LV, KV and HH acknowledge DFG project number HA 1344/45-1. LJF acknowledges support from the Alexander von Humboldt Foundation, Bonn, Germany. This publication is part of the project ‘High entropy oxide electrocatalysts’ (with project number KICH1.ED04.20.003) of the research programme ECCM KICkstart DE-NL which is (partly) financed by the Dutch Research Council (NWO).

ACKNOWLEDGMENT

The authors thank Qiyang Lu, Monica Morales Masis and Marco Altomare for critical discussion and Minh Nguyen, Shreyas Harsha and Tursun Abudukade for help in sample fabrication and Karin van den Nieuwenhuijzen for XRD measurements. LV thanks the Karlsruhe Nano Micro Facility (KNMF, Germany) and Prof. Christian Kübel for providing access to TEM at KIT. This research used beamline 9.3.2 of the Advanced Light Source, a U.S. DOE Office of Science User Facility under contract no. DE-AC02-05CH11231.

REFERENCES

(1) Beall, C. E.; Fabbri, E.; Schmidt, T. J. Perovskite Oxide Based Electrodes for the Oxygen Reduction and Evolution Reactions: The Underlying Mechanism. *ACS Catal.* **2021**, *11* (5), 3094–3114. https://doi.org/10.1021/acscatal.0c04473.

(2) Fabbri, E.; Schmidt, T. J. Oxygen Evolution Reaction—The Enigma in Water Electrolysis. *ACS Catal.* **2018**, *8* (10), 9765–9774. https://doi.org/10.1021/acscatal.8b02712.

(3) Man, I. C.; Su, H.-Y.; Calle-Vallejo, F.; Hansen, H. A.; Martínez, J. I.; Inoglu, N. G.; Kitchin, J.; Jaramillo, T. F.; Nørskov, J. K.; Rossmeisl, J.; Calle-Vallejo, F.; Hansen, H. A.; Martínez, J. I.; Inoglu, N. G.; Kitchin, J.; Jaramillo, T. F.; Nørskov, J. K.; Rossmeisl, J. Universality in Oxygen Evolution Electrocatalysis on Oxide Surfaces. *ChemCatChem* **2011**, *3* (7), 1159–1165. https://doi.org/10.1002/cctc.201000397.

(4) Rossmeisl, J.; Logadottir, A.; Nørskov, J. K. Electrolysis of Water on (Oxidized) Metal Surfaces. *Chem. Phys.* **2005**, *319* (1–3), 178–184. https://doi.org/10.1016/j.chemphys.2005.05.038.

(5) Seh, Z. W.; Kibsgaard, J.; Dickens, C. F.; Chorkendorff, I.; Nørskov, J. K.; Jaramillo, T. F. Combining Theory and Experiment in Electrocatalysis: Insights into Materials Design. *Science (80-.).* **2017**, *355* (6321), eaad4998. https://doi.org/10.1126/science.aad4998.

(6) Suntivich, J.; May, K. J.; Gasteiger, H. a.; Goodenough, J. B.; Shao-Horn, Y. A Perovskite Oxide Optimized for Molecular Orbital Principles - Supporting Online Material. *Science (80-.).* **2011**, *334* (December), 2010–2012. https://doi.org/10.1126/science.1212858.

(7) Kulkarni, A.; Siahrostami, S.; Patel, A.; Nørskov, J. K. Understanding Catalytic Activity Trends in the Oxygen Reduction Reaction. *Chem. Rev.* **2018**, *118* (5), 2302–2312. https://doi.org/10.1021/acs.chemrev.7b00488.

(8) Bockris, J. O. The Electrocatalysis of Oxygen Evolution on Perovskites. *J. Electrochem. Soc.* **1984**, *131* (2), 290. https://doi.org/10.1149/1.2115565.

(9) Antipin, D.; Risch, M. Trends of Epitaxial Perovskite Oxide Films Catalyzing the Oxygen Evolution Reaction in Alkaline Media. *J. Phys. Energy* **2020**, *2* (3), 032003. https://doi.org/10.1088/2515-7655/ab812f.

(10) Risch, M.; Stoerzinger, K. A.; Maruyama, S.; Hong, W. T.; Takeuchi, I.; Shao-Horn, Y. $La_{0.8}Sr_{0.2}MnO_{3-\delta}$ Decorated with $Ba_{0.5}Sr_{0.5}Co_{0.8}Fe_{0.2}O_{3-\delta}$: A Bifunctional Surface for Oxygen Electrocatalysis with Enhanced Stability and Activity. *J. Am. Chem. Soc.* **2014**, *136* (14), 5229–5232. https://doi.org/10.1021/ja5009954.

(11) Wang, L.; Adiga, P.; Zhao, J.; Samarakoon, W. S.; Stoerzinger, K. A.; Spurgeon, S. R.; Matthews, B. E.; Bowden, M. E.; Sushko, P. V; Kaspar, T. C.; Sterbinsky, G. E.; Heald, S. M.; Wang, H.; Wangoh, L. W.; Wu, J.; Guo, E.; Qian, H.; Wang, J.; Varga, T.; Thevuthasan, S.; Feng, Z.; Yang, W.; Du, Y.; Chambers, S. A. Understanding the Electronic Structure Evolution of Epitaxial LaNi 1– x Fe x O 3 Thin Films for Water Oxidation. *Nano Lett.* **2021**, *21* (19), 8324–8331. https://doi.org/10.1021/acs.nanolett.1c02901.

(12) Baeumer, C.; Li, J.; Lu, Q.; Liang, A. Y.-L.; Jin, L.; Martins, H. P.; Duchoň, T.; Glöß, M.; Gericke, S. M.; Wohlgemuth, M. A.; Giesen, M.; Penn, E. E.; Dittmann, R.; Gunkel, F.; Waser, R.; Bajdich, M.; Nemšák, S.; Mefford, J. T. T.; Chueh, W. C. Tuning

Electrochemically Driven Surface Transformation in Atomically Flat LaNiO3 Thin Films for Enhanced Water Electrolysis. *Nat. Mater.* **2021**, *20* (5), 674–682. https://doi.org/10.1038/s41563-020-00877-1.

(13) Bockris, J. O.; Otagawa, T. Mechanism of Oxygen Evolution on Perovskites. *J. Phys. Chem.* **1983**, *87* (15), 2960–2971. https://doi.org/10.1021/j100238a048.

(14) Wang, L.; Stoerzinger, K. A.; Chang, L.; Zhao, J.; Li, Y.; Tang, C. S.; Yin, X.; Bowden, M. E.; Yang, Z.; Guo, H.; You, L.; Guo, R.; Wang, J.; Ibrahim, K.; Chen, J.; Rusydi, A.; Wang, J.; Chambers, S. A.; Du, Y. Tuning Bifunctional Oxygen Electrocatalysts by Changing the A-Site Rare-Earth Element in Perovskite Nickelates. *Adv. Funct. Mater.* **2018**, *28* (39), 1803712. https://doi.org/10.1002/adfm.201803712.

(15) Batchelor, T. A. A.; Löffler, T.; Xiao, B.; Krysiak, O. A.; Strotkötter, V.; Pedersen, J. K.; Clausen, C. M.; Savan, A.; Li, Y.; Schuhmann, W.; Rossmeisl, J.; Ludwig, A. Complex-Solid-Solution Electrocatalyst Discovery by Computational Prediction and High-Throughput Experimentation**. *Angew. Chemie Int. Ed.* **2021**, *60* (13), 6932–6937. https://doi.org/10.1002/anie.202014374.

(16) Batchelor, T. A. A.; Pedersen, J. K.; Winther, S. H.; Castelli, I. E.; Jacobsen, K. W.; Rossmeisl, J. High-Entropy Alloys as a Discovery Platform for Electrocatalysis. *Joule* **2019**, *3* (3), 834–845. https://doi.org/10.1016/j.joule.2018.12.015.

(17) Banko, L.; Krysiak, O. A.; Pedersen, J. K.; Xiao, B.; Savan, A.; Löffler, T.; Baha, S.; Rossmeisl, J.; Schuhmann, W.; Ludwig, A. Unravelling Composition–Activity–Stability Trends in High Entropy Alloy Electrocatalysts by Using a Data-Guided Combinatorial Synthesis Strategy and Computational Modeling. *Adv. Energy Mater.* **2022**, *2103312*, 2103312. https://doi.org/10.1002/aenm.202103312.

(18) Löffler, T.; Ludwig, A.; Rossmeisl, J.; Schuhmann, W. What Makes High-Entropy Alloys Exceptional Electrocatalysts? *Angew. Chemie Int. Ed.* **2021**, *60* (52), 26894–26903. https://doi.org/10.1002/anie.202109212.

(19) Chen, Z.; Zhang, T.; Gao, X.; Huang, Y.; Qin, X.; Wang, Y.; Zhao, K.; Peng, X.; Zhang, C.; Liu, L.; Zeng, M.; Yu, H. Engineering Microdomains of Oxides in High-Entropy Alloy Electrodes toward Efficient Oxygen Evolution. *Adv. Mater.* **2021**, *33* (33), 2101845. https://doi.org/10.1002/adma.202101845.

(20) Yang, X.; Guo, R.; Cai, R.; Ouyang, Y.; Yang, P.; Xiao, J. Engineering High-Entropy Materials for Electrocatalytic Water Splitting. *Int. J. Hydrogen Energy* **2022**, No. xxxx. https://doi.org/10.1016/j.ijhydene.2022.02.123.

(21) Trotochaud, L.; Ranney, J. K.; Williams, K. N.; Boettcher, S. W. Solution-Cast Metal Oxide Thin Film Electrocatalysts for Oxygen Evolution. *J. Am. Chem. Soc.* **2012**, *134* (41), 17253–17261. https://doi.org/10.1021/ja307507a.

(22) Sarkar, A.; Djenadic, R.; Wang, D.; Hein, C.; Kautenburger, R.; Clemens, O.; Hahn, H. Rare Earth and Transition Metal Based Entropy Stabilised Perovskite Type Oxides. *J. Eur. Ceram. Soc.* **2018**, *38* (5), 2318–2327. https://doi.org/10.1016/j.jeurceramsoc.2017.12.058.

(23) Sarkar, A.; Wang, Q.; Schiele, A.; Chellali, M. R.; Bhattacharya, S. S.; Wang, D.; Brezesinski, T.; Hahn, H.; Velasco, L.; Breitung, B. High-Entropy Oxides: Fundamental Aspects and Electrochemical Properties. *Adv. Mater.* **2019**, *31* (26), 1806236.

https://doi.org/10.1002/adma.201806236.

(24) Sharma, Y.; Zheng, Q.; Mazza, A. R.; Skoropata, E.; Heitmann, T.; Gai, Z.; Musico, B.; Miceli, P. F.; Sales, B. C.; Keppens, V.; Brahlek, M.; Ward, T. Z. Magnetic Anisotropy in Single-Crystal High-Entropy Perovskite Oxide $La(Cr_{0.2}Mn_{0.2}Fe_{0.2}Co_{0.2}Ni_{0.2})O_3$ Film. *Phys. Rev. Mater.* **2020**, *4* (1), 014404. https://doi.org/10.1103/PhysRevMaterials.4.014404.

(25) Heymann, L.; Weber, M. L.; Wohlgemuth, M.; Risch, M.; Dittmann, R.; Baeumer, C.; Gunkel, F. Separating the Effects of Band Bending and Covalency in Hybrid Perovskite Oxide Electrocatalyst Bilayers for Water Electrolysis. *ACS Appl. Mater. Interfaces* **2022**, *14* (12), 14129–14136. https://doi.org/10.1021/acsami.1c20337.

(26) Mefford, J. T.; Rong, X.; Abakumov, A. M.; Hardin, W. G.; Dai, S.; Kolpak, A. M.; Johnston, K. P.; Stevenson, K. J. Water Electrolysis on $La_{1-x}Sr_xCoO_{3-\delta}$ Perovskite Electrocatalysts. *Nat. Commun.* **2016**, *7*, 11053. https://doi.org/10.1038/ncomms11053.

(27) Hong, W. T.; Stoerzinger, K. A.; Lee, Y.-L.; Giordano, L.; Grimaud, A.; Johnson, A. M.; Hwang, J.; Crumlin, E. J.; Yang, W.; Shao-Horn, Y. Charge-Transfer-Energy-Dependent Oxygen Evolution Reaction Mechanisms for Perovskite Oxides. *Energy Environ. Sci.* **2017**, *10* (10), 2190–2200. https://doi.org/10.1039/C7EE02052J.

(28) Tang, L.; Yang, Y.; Guo, H.; Wang, Y.; Wang, M.; Liu, Z.; Yang, G.; Fu, X.; Luo, Y.; Jiang, C.; Zhao, Y.; Shao, Z.; Sun, Y. High Configuration Entropy Activated Lattice Oxygen for O_2 Formation on Perovskite Electrocatalyst. *Adv. Funct. Mater.* **2022**, 2112157. https://doi.org/10.1002/adfm.202112157.

(29) Sarkar, A.; Velasco, L.; Wang, D.; Wang, Q.; Talasila, G.; de Biasi, L.; Kübel, C.; Brezesinski, T.; Bhattacharya, S. S.; Hahn, H.; Breitung, B. High Entropy Oxides for Reversible Energy Storage. *Nat. Commun.* **2018**, *9* (1), 3400. https://doi.org/10.1038/s41467-018-05774-5.

(30) Baiutti, F.; Chiabrera, F.; Acosta, M.; Diercks, D.; Parfitt, D.; Santiso, J.; Wang, X.; Cavallaro, A.; Morata, A.; Wang, H.; Chroneos, A.; MacManus-Driscoll, J.; Tarancon, A. A High-Entropy Manganite in an Ordered Nanocomposite for Long-Term Application in Solid Oxide Cells. *Nat. Commun.* **2021**, *12* (1), 2660. https://doi.org/10.1038/s41467-021-22916-4.

(31) Amiri, A.; Shahbazian-Yassar, R. Recent Progress of High-Entropy Materials for Energy Storage and Conversion. *J. Mater. Chem. A* **2021**, *9* (2), 782–823. https://doi.org/10.1039/d0ta09578h.

(32) Albedwawi, S. H.; AlJaberi, A.; Haidemenopoulos, G. N.; Polychronopoulou, K. High Entropy Oxides-Exploring a Paradigm of Promising Catalysts: A Review. *Mater. Des.* **2021**, *202*, 109534. https://doi.org/10.1016/j.matdes.2021.109534.

(33) Jiang, S.; Hu, T.; Gild, J.; Zhou, N.; Nie, J.; Qin, M.; Harrington, T.; Vecchio, K.; Luo, J. A New Class of High-Entropy Perovskite Oxides. *Scr. Mater.* **2018**, *142*, 116–120. https://doi.org/10.1016/j.scriptamat.2017.08.040.

(34) Nguyen, T. X.; Liao, Y.; Lin, C.; Su, Y.; Ting, J. Advanced High Entropy Perovskite Oxide Electrocatalyst for Oxygen Evolution Reaction. *Adv. Funct. Mater.* **2021**, *31* (27), 2101632. https://doi.org/10.1002/adfm.202101632.

(35) Zhang, L.; Cai, W.; Bao, N. Top-Level Design Strategy to Construct an Advanced High-Entropy Co–Cu–Fe–Mo (Oxy)Hydroxide Electrocatalyst for the Oxygen Evolution Reaction. *Adv. Mater.* **2021**, *33* (22), 2100745. https://doi.org/10.1002/adma.202100745.

(36) Stamenkovic, V. R.; Strmcnik, D.; Lopes, P. P.; Markovic, N. M. Energy and Fuels from Electrochemical Interfaces. *Nat. Mater.* **2017**, *16* (1), 57–69. https://doi.org/10.1038/nmat4738.

(37) Yang, X.; Guo, R.; Cai, R.; Ouyang, Y.; Yang, P.; Xiao, J. Engineering High-Entropy Materials for Electrocatalytic Water Splitting. *Int. J. Hydrogen Energy* **2022**, *47* (28), 13561–13578. https://doi.org/10.1016/j.ijhydene.2022.02.123.

(38) Weber, M. L.; Gunkel, F. Epitaxial Catalysts for Oxygen Evolution Reaction: Model Systems and Beyond. *J. Phys. Energy* **2019**, *1* (3), 031001. https://doi.org/10.1088/2515-7655/ab1577.

(39) Mefford, J. T.; Kurilovich, A. A.; Saunders, J.; Hardin, W. G.; Abakumov, A. M.; Forslund, R. P.; Bonnefont, A.; Dai, S.; Johnston, K. P.; Stevenson, K. J. Decoupling the Roles of Carbon and Metal Oxides on the Electrocatalytic Reduction of Oxygen on $La_{1-x}Sr_xCoO_{3-\delta}$ Perovskite Composite Electrodes. *Phys. Chem. Chem. Phys.* **2019**, *21* (6), 3327–3338. https://doi.org/10.1039/C8CP06268D.

(40) Tkalych, A. J.; Zhuang, H. L.; Carter, E. A. A Density Functional + U Assessment of Oxygen Evolution Reaction Mechanisms on β-NiOOH. *ACS Catal.* **2017**, *7* (8), 5329–5339. https://doi.org/10.1021/acscatal.7b00999.

(41) Baeumer, C.; Xu, C.; Gunkel, F.; Raab, N.; Heinen, R. A.; Koehl, A.; Dittmann, R. Surface Termination Conversion during $SrTiO_3$ Thin Film Growth Revealed by X-Ray Photoelectron Spectroscopy. *Sci. Rep.* **2015**, *5* (1), 11829. https://doi.org/10.1038/srep11829.

(42) Weber, M. L.; Baeumer, C.; Mueller, D. N.; Jin, L.; Jia, C.-L.; Bick, D. S.; Waser, R.; Dittmann, R.; Valov, I.; Gunkel, F. Electrolysis of Water at Atomically Tailored Epitaxial Cobaltite Surfaces. *Chem. Mater.* **2019**, *31* (7), 2337–2346. https://doi.org/10.1021/acs.chemmater.8b04577.

(43) Daulton, T. L.; Little, B. J. Determination of Chromium Valence over the Range Cr(0)–Cr(VI) by Electron Energy Loss Spectroscopy. *Ultramicroscopy* **2006**, *106* (7), 561–573. https://doi.org/10.1016/j.ultramic.2006.02.005.

(44) Wang, Z. L.; Yin, J. S.; Jiang, Y. D. EELS Analysis of Cation Valence States and Oxygen Vacancies in Magnetic Oxides. *Micron* **2000**, *31* (5), 571–580. https://doi.org/10.1016/S0968-4328(99)00139-0.

(45) Tan, H.; Verbeeck, J.; Abakumov, A.; Van Tendeloo, G. Oxidation State and Chemical Shift Investigation in Transition Metal Oxides by EELS. *Ultramicroscopy* **2012**, *116* (2012), 24–33. https://doi.org/10.1016/j.ultramic.2012.03.002.

(46) Zhong, Z.; Hansmann, P. Band Alignment and Charge Transfer in Complex Oxide Interfaces. *Phys. Rev. X* **2017**, *7* (1), 011023. https://doi.org/10.1103/PhysRevX.7.011023.

(47) Gunkel, F.; Christensen, D. V.; Chen, Y. Z.; Pryds, N. Oxygen Vacancies: The (in)Visible Friend of Oxide Electronics. *Appl. Phys. Lett.* **2020**, *116* (12), 120505.

https://doi.org/10.1063/1.5143309.

(48) Hobbs, C.; Downing, C.; Jaskaniec, S.; Nicolosi, V. TEM and EELS Characterization of Ni–Fe Layered Double Hydroxide Decompositions Caused by Electron Beam Irradiation. *npj 2D Mater. Appl.* **2021**, *5* (1), 29. https://doi.org/10.1038/s41699-021-00212-5.

(49) Yoo, J. S.; Rong, X.; Liu, Y.; Kolpak, A. M. Role of Lattice Oxygen Participation in Understanding Trends in the Oxygen Evolution Reaction on Perovskites. *ACS Catal.* **2018**, *8* (5), 4628–4636. https://doi.org/10.1021/acscatal.8b00612.

(50) Hong, W. T.; Stoerzinger, K. A.; Moritz, B.; Devereaux, T. P.; Yang, W.; Shao-Horn, Y. Probing LaMO 3 Metal and Oxygen Partial Density of States Using X-Ray Emission, Absorption, and Photoelectron Spectroscopy. *J. Phys. Chem. C* **2015**, *119* (4), 2063–2072. https://doi.org/10.1021/jp511931y.

(51) Grimaud, A.; May, K. J.; Carlton, C. E.; Lee, Y.-L.; Risch, M.; Hong, W. T.; Zhou, J.; Shao-Horn, Y. Double Perovskites as a Family of Highly Active Catalysts for Oxygen Evolution in Alkaline Solution. *Nat. Commun.* **2013**, *4* (1), 2439. https://doi.org/10.1038/ncomms3439.

(52) Song, J.; Wei, C.; Huang, Z.-F.; Liu, C.; Zeng, L.; Wang, X.; Xu, Z. J. A Review on Fundamentals for Designing Oxygen Evolution Electrocatalysts. *Chem. Soc. Rev.* **2020**, *49* (7), 2196–2214. https://doi.org/10.1039/C9CS00607A.

(53) Dionigi, F.; Zeng, Z.; Sinev, I.; Merzdorf, T.; Deshpande, S.; Lopez, M. B.; Kunze, S.; Zegkinoglou, I.; Sarodnik, H.; Fan, D.; Bergmann, A.; Drnec, J.; Araujo, J. F. de; Gliech, M.; Teschner, D.; Zhu, J.; Li, W.-X.; Greeley, J.; Cuenya, B. R.; Strasser, P. In-Situ Structure and Catalytic Mechanism of NiFe and CoFe Layered Double Hydroxides during Oxygen Evolution. *Nat. Commun.* **2020**, *11* (1), 2522. https://doi.org/10.1038/s41467-020-16237-1.

(54) Carvalho, O. Q.; Adiga, P.; Wang, L.; Liu, J.; Jia, E.; Du, Y.; Nemšák, S.; Stoerzinger, K. A. Probing Adsorbates on La 1−x Sr x NiO 3−δ Surfaces under Humid Conditions: Implications for the Oxygen Evolution Reaction. *J. Phys. D. Appl. Phys.* **2021**, *54* (27), 274003. https://doi.org/10.1088/1361-6463/abf674.

(55) Nong, H. N.; Falling, L. J.; Bergmann, A.; Klingenhof, M.; Tran, H. P.; Spöri, C.; Mom, R.; Timoshenko, J.; Zichittella, G.; Knop-Gericke, A.; Piccinin, S.; Pérez-Ramírez, J.; Cuenya, B. R.; Schlögl, R.; Strasser, P.; Teschner, D.; Jones, T. E. Key Role of Chemistry versus Bias in Electrocatalytic Oxygen Evolution. *Nature* **2020**, *587* (7834), 408–413. https://doi.org/10.1038/s41586-020-2908-2.

(56) Chung, D. Y.; Lopes, P. P.; Farinazzo Bergamo Dias Martins, P.; He, H.; Kawaguchi, T.; Zapol, P.; You, H.; Tripkovic, D.; Strmcnik, D.; Zhu, Y.; Seifert, S.; Lee, S.; Stamenkovic, V. R.; Markovic, N. M. Dynamic Stability of Active Sites in Hydr(Oxy)Oxides for the Oxygen Evolution Reaction. *Nat. Energy* **2020**, *5* (3), 222–230. https://doi.org/10.1038/s41560-020-0576-y.

(57) Stoerzinger, K. A.; Renshaw Wang, X.; Hwang, J.; Rao, R. R.; Hong, W. T.; Rouleau, C. M.; Lee, D.; Yu, Y.; Crumlin, E. J.; Shao-Horn, Y. Speciation and Electronic Structure of La1−xSrxCoO3−δ During Oxygen Electrolysis. *Top. Catal.* **2018**, *61* (20), 2161–2174. https://doi.org/10.1007/s11244-018-1070-7.

(58) Qiao, L.; Droubavy, T. C.; Bowden, M. E.; Shutthanandan, V.; Kaspar, T. C.; Chambers, S. A. LaCrO 3 Heteroepitaxy on SrTiO 3 (001) by Molecular Beam Epitaxy. *Appl. Phys. Lett.* **2011**, *99* (6), 061904. https://doi.org/10.1063/1.3624473.

(59) Singh, R. N.; Singh, J. P.; Lal, B.; Thomas, M. J. K.; Bera, S. New NiFe2−xCrxO4 Spinel Films for O2 Evolution in Alkaline Solutions. *Electrochim. Acta* **2006**, *51* (25), 5515–5523. https://doi.org/10.1016/j.electacta.2006.02.028.

(60) Gracia, J. Spin Dependent Interactions Catalyse the Oxygen Electrochemistry. *Phys. Chem. Chem. Phys.* **2017**, *19* (31), 20451–20456. https://doi.org/10.1039/C7CP04289B.

(61) Velasco, L.; Castillo, J. S.; Kante, M. V.; Olaya, J. J.; Friederich, P.; Hahn, H. Phase–Property Diagrams for Multicomponent Oxide Systems toward Materials Libraries. *Adv. Mater.* **2021**, *33* (43), 2102301. https://doi.org/10.1002/adma.202102301.

(62) Tanuma, S.; Powell, C. J.; Penn, D. R. Calculations of Electron Inelastic Mean Free Paths. V. Data for 14 Organic Compounds over the 50-2000 EV Range. *Surf. Interface Anal.* **1994**, *21* (3), 165–176. https://doi.org/10.1002/sia.740210302.

(63) Powell, C. J. Practical Guide for Inelastic Mean Free Paths, Effective Attenuation Lengths, Mean Escape Depths, and Information Depths in x-Ray Photoelectron Spectroscopy. *J. Vac. Sci. Technol. A* **2020**, *38* (2), 023209. https://doi.org/10.1116/1.5141079.

(64) Jablonski, A.; Powell, C. J. Practical Expressions for the Mean Escape Depth, the Information Depth, and the Effective Attenuation Length in Auger-Electron Spectroscopy and x-Ray Photoelectron Spectroscopy. *J. Vac. Sci. Technol. A Vacuum, Surfaces, Film.* **2009**, *27* (2), 253–261. https://doi.org/10.1116/1.3071947.

(65) Chambers, S. A.; Du, Y. Experimental Determination of Electron Attenuation Lengths in Complex Materials by Means of Epitaxial Film Growth: Advantages and Challenges. *J. Vac. Sci. Technol. A* **2020**, *38* (4), 043409. https://doi.org/10.1116/6.0000291.

(66) Chellali, M. R.; Sarkar, A.; Nandam, S. H.; Bhattacharya, S. S.; Breitung, B.; Hahn, H.; Velasco, L. On the Homogeneity of High Entropy Oxides: An Investigation at the Atomic Scale. *Scr. Mater.* **2019**, *166* (February), 58–63. https://doi.org/10.1016/j.scriptamat.2019.02.039.

(67) Wei, C.; Rao, R. R.; Peng, J.; Huang, B.; Stephens, I. E. L.; Risch, M.; Xu, Z. J.; Shao-Horn, Y. Recommended Practices and Benchmark Activity for Hydrogen and Oxygen Electrocatalysis in Water Splitting and Fuel Cells. *Adv. Mater.* **2019**, *31* (31), 1806296. https://doi.org/10.1002/adma.201806296.